



# Uniform Microstructure and Excellent Corrosion Resistance of HVOF-Sprayed CoCrNi Medium-Entropy Alloy Coating in Fluoride Ion Environment

Dongbao Huang<sup>1,2</sup> · Zhenlin Xu<sup>1,3</sup> · Xiquan Jia<sup>1</sup> · Haitao Yu<sup>1</sup> · Yizhu He<sup>1,3</sup>  · Zhenqi Dong<sup>2</sup> · Shenshen Li<sup>2</sup> · Hui Zhang<sup>1</sup>

Received: 30 January 2023 / Accepted: 25 May 2023 / Published online: 1 July 2023  
© The Author(s) under exclusive licence to The Korean Institute of Metals and Materials 2023

## Abstract

To solve the corrosion problem of the copper plates caused by fluoride ions, the Ni55 and CoCrNi medium-entropy alloy coatings were prepared via high-velocity oxygen fuel technology. The corrosion resistance of the Ni55 and CoCrNi coatings in NaF solution was compared through electrochemical experiments and immersion corrosion experiments. The Ni55 coating contained complex precipitated phases, resulting in preferential corrosion at the phase boundaries between the  $\gamma$ -Ni solid solution and the precipitated phases. The composition of the CoCrNi coating was more homogeneously distributed, and mainly uniform corrosion occurred. The corrosion products of the two coatings in the NaF solution were both complexes composed of metal oxides and fluorides. Compared with the Ni55 coating, the passive film formed on the CoCrNi coating had a more uniform and protective property; therefore, the CoCrNi coating had better corrosion resistance. This research can pave a pathway for developing coating on copper and its alloys with excellent corrosion resistance.

**Keywords** Corrosion resistance · Microstructure · Medium-entropy alloy · HVOF · Coating

## 1 Introduction

Copper and its alloys have a good combination of excellent thermal conductivity, good plasticity, and workability [1, 2]. Therefore, they are widely used in chemical, aviation, and metallurgy industries, such as mold copper plates in the continuous casting process [3, 4]. The mold is the core component of the steel-making and continuous casting equipment, which directly affects the quality of the billet steel. During the continuous casting process, corrosion is one of the main failure modes of the mold copper plate [5,

6]. Under ideal conditions, the mold copper plate is close to the solid protective slag layer (components of  $\text{Na}_2\text{O}$ ,  $\text{CaF}_2$ ,  $\text{SiO}_2$ ,  $\text{Al}_2\text{O}_3$ , etc.). However, in the actual production process, because of production fluctuations or equipment, there will be a gap between the mold copper plate and the protective slag layer. At the same time, the protective slag reacts at high temperatures to generate fluoride salt, such as the reaction of  $\text{CaF}_2$  and  $\text{Na}_2\text{O}$  to generate NaF gas. If there is water vapor in the gap, a corrosion cell with the copper plate as the anode and the cast billet as the cathode will be formed, causing the electrochemical corrosion of the surface of the copper plate [7, 8].

The preparation of coatings on the working surface of the mold copper plate through electroplating, laser cladding, and thermal spraying is the primary way to extend its service life [9–11]. The electroplating method is the most mature and widely used technology. Due to the low temperature of the electroplating solution ( $< 100\text{ }^\circ\text{C}$ ), the adverse effect of high temperature on the substrate material and the coating can be effectively avoided [12]. However, the electroplating layer has a long deposition cycle and low hardness, and the coating easily falls off [6]. At the same time, electroplating technology is very polluting to the environment, so

✉ Yizhu He  
heyizhu@ahut.edu.cn

Dongbao Huang  
huangdongbao@taiergroup.com

<sup>1</sup> School of Materials Science and Engineering, Anhui University of Technology, Maanshan 243002, China

<sup>2</sup> Taier (Anhui) Industrial Technology and Service Limited Company, Maanshan 243000, China

<sup>3</sup> Anhui Key Lab of Metal Material and Processing, Maanshan 243002, China

the elimination of electroplating technology has become an inevitable trend. Owing to the significant difference in thermal conductivity between copper and alloy coatings, coatings fabricated using laser cladding generally have high residual stress and cracking problems, which are difficult to apply in industrial production [4, 13]. As one of the most widely used thermal spraying techniques, high-velocity oxygen fuel (HVOF) can prepare high-density and uniform coatings, as a result of its fast flame flow rate, high powder kinetic energy, and low oxidation [14, 15]. In addition, the HVOF technology has a wide range of material choices. It can be designed for different sizes and positions of the mold to meet the requirements of continuous casting conditions.

Ni-based alloy has been applied to the industrialized preparation of HVOF coatings on mold copper plates due to its good corrosion resistance and mechanical properties. Compared with electroplated coatings, the HVOF Ni-based alloy coatings generally have better wear resistance [15–17]. However, the precipitated phases, such as borides and carbides, in the Ni-based alloy coating are not conducive to further enhancing the corrosion resistance [18, 19]. Because of the difference in self-corrosion potential, the interface between the precipitated phase and the Ni-based alloy matrix is more susceptible to corrosion. Yang et al. [20] researched the distribution of the anodic and cathodic activities on the surface of the local electrochemical corrosion of a thermal-sprayed Ni60 coating. As a consequence of the presence of the precipitated phases, the coating has large and dense anode potential microregions, and the corrosion of these microregions was more serious. Pan et al. [21] studied the corrosion behavior of a TiC particle-reinforced Ni60 coating in an aluminum alloy melt. Corrosion cracks of the coating originated at the junction of TiC and  $\gamma$ -Ni at the corrosion front and propagated in the  $\gamma$ -Ni matrix. Laser remelting treatment of the  $\text{Cr}_3\text{C}_2$ -NiCr coating could promote the nucleation and uniform distribution of carbides, inhibiting the galvanic corrosion between the alloy matrix and the carbides, thereby improving the coating's resistance to the NaCl solution [22]. Therefore, finding and developing new corrosion-resistant alloy materials for HVOF is an urgent bottleneck problem to be solved.

Medium-entropy/high-entropy alloys (MEAs/HEAs) are multi-component advanced alloys that are designed based on the concept of entropy control, have no principal elements, and are structurally ordered and chemically disordered. MEAs/HEAs exhibit excellent corrosion resistance, mechanical properties, and high-temperature oxidation resistance [23–25]. The MEA not only has the excellent properties of the HEA but also has a relatively low number of principal elements, and the preparation cost is often lower than that of the HEA. Among them, the equiatomic CoCrNi MEA with a face-centered cubic (FCC) structure has great application potential and has become one of the research hotspots in

recent years [26]. Compared with the typical CoCrFeMnNi HEA, the CoCrNi MEA has higher strength, which is related to the occurrence of a stress-induced FCC-HCP phase transition because of its lower stacking fault energy [25, 27]. Besides, the CoCrNi MEA has good high-temperature wear resistance. When the temperature exceeded 200 °C, the wear rate of the CoCrNi MEA was lower than that of the 718 Ni-based alloy [28]. This is because the wear surface of the CoCrNi MEA formed a composite structure with high-density dislocation cells, nanoscale deformation twins, and a large number of stacking faults, thereby reducing the friction coefficient and improving the wear resistance.

Studies have shown that the corrosion resistance of the CoCrNi MEA was superior to that of the conventional corrosion-resistant material. In the NaCl solution or the  $\text{H}_2\text{SO}_4$  solution, the corrosion resistance of the CoCrNi MEA was better than that of the 316 L and 304 stainless steel [29–31]. Different preparation processes significantly affect the microstructure of the alloy, thereby affecting its corrosion resistance. At present, the preparation techniques of the CoCrNi MEA mainly involve vacuum melting, rolling, and laser additive manufacturing. At present, there are few reports about thermally sprayed CoCrNi coatings. Koga et al. [32] studied the electrochemical corrosion resistance of the  $\text{Cr}_{40}\text{Co}_{40}\text{Ni}_{20}$  coatings prepared by HVOF and high-velocity air fuel (HVOF). The formation of spinel and oxide during coating deposition led to the Cr-depletion region, which reduced the corrosion resistance of coating in NaCl solution. Furthermore, the corrosion resistance of the CoCrNi MEA was mainly studied using NaCl,  $\text{H}_2\text{SO}_4$ , and NaOH solutions as the corrosion medium. Although fluorine and chlorine belong to the same group of halogen elements, the influencing mechanisms of fluoride and chloride ions on the corrosion behavior of metals are different. For example, stainless steel was mainly pitted in a chloride-ion environment. In contrast, fluoride ions could cause intergranular corrosion, and fluoride ions had a more potent destructive force on the passive film [33]. The corrosion behavior of CoCrNi alloys and Ni-based alloys in fluoride salt solution has not been reported, and the corrosion mechanism is still not precise.

In this study, the Ni55 and the equiatomic CoCrNi coatings were prepared on the surface of the mold copper plates using the HVOF technique. Then, the corrosion behavior of the two coatings in the 3.5 wt% NaF solution was compared through the electrochemical experiment and the immersion corrosion experiment. The composition of the passive films formed on the two coatings was investigated via X-ray photoelectron spectroscopy (XPS). This study benefits the development of long-life coatings for mold copper plates and the optimization of corrosion-resistant coating in other fields.

## 2 Experimental Materials and Methods

The CuCrZr alloy with a chemical composition of 98.8Cu-1.00Cr-0.20Zr in weight percentages was used as the substrate material. The sprayed powders were spherical Ni55 and CoCrNi powders prepared by gas atomization, and the process parameters used for powder production are listed in Table 1. The particle size distribution of the powders was 15–53  $\mu\text{m}$ , and Table 2 details their chemical compositions measured by inductively coupled plasma optical emission spectrometry (ICP-OES). The Ni55 and CoCrNi coatings were processed onto 30 mm  $\times$  50 mm CuCrZr substrates by the HVOF system (Praxair JP8000). Before spraying, the substrate surface was subjected to sandblasting and acetone cleaning. The main process parameters of the HVOF are as follows: kerosene flow rate of 26 L/h, oxygen flow rate of 53  $\text{m}^3/\text{h}$ , spraying distance of 350 mm, and powder supply rate of 70 g/min. A tube furnace was used to heat the sprayed samples to 1000  $^\circ\text{C}$  and keep it for four h, and then they were cooled with the furnace.

The prepared specimens were coarsely ground, finely ground, and polished. The phase constitutes of the coatings was characterized using an X-ray diffractometer (XRD, D/max2500pcX) equipped with a Cu target. The scanning step was 0.02 $^\circ$ , the counting time was 2 s, the test voltage was 40 kV, and the test current was 200 mA. The microstructure observation of the coating was performed utilizing scanning electron microscopy (SEM, JSM-7001F) and electron backscatter diffraction (EBSD). The EBSD data were analyzed using the Oxford HKL Channel5 software. The element distribution of the coating was measured by an energy spectrum analyzer (EDS) attached to the SEM equipment. A transmission electron microscope (TEM, Zeiss libra 200) operated at 200 kV was employed to observe the nanoscale microstructure of the coatings.

The CHI-760D electrochemical workstation with a three-electrode system was employed for the electrochemical test in a 3.5 wt% NaF solution at 25  $^\circ\text{C}$ , using the sample as the working electrode, the saturated calomel electrode (SCE) as the reference electrode, and the platinum plate as the counter electrode. The open circuit potential (OCP) test time was 60 min to obtain a very stable value. The initial potential of the potentiodynamic polarization curve test was  $-0.9 V_{\text{SCE}}$ , the final potential was  $1.1 V_{\text{SCE}}$ , and the scanning rate was 1 mV/s. The frequency of the electrochemical impedance spectrum (EIS) test was 0.01 Hz to 100 kHz under the OCP condition, and the voltage amplitude was 10 mV. The EIS data were fitted and analyzed using Zview software. To ensure the accuracy of the results, each test was carried out more than three times.

To investigate the composition of the passive film, the sample was passivated at a potential of  $0.4 V_{\text{SCE}}$  for 1 h in

the 3.5 wt% NaF solution to form a stable passive film. The composition of the passive film was examined by X-ray photoelectron spectroscopy (XPS, Thermo Scientific K-Alpha) with an  $\text{Al}_{K\alpha}$  radiation source. In the XPS test, the standard peak of C was used for calibration (C1 s, 284.8 eV), and the XPS data analysis was conducted by Avantage software. Then the specimens were immersed in a 3.5 wt% NaF solution for 7 days at room temperature. Then, the corrosion morphology was detected using a laser confocal microscope and an SEM, and the composition of the corrosion products was investigated using the EDS.

## 3 Results and Discussion

### 3.1 Microstructure Characterization

Figure 1 exhibits the X-ray diffraction patterns of the Ni55 and CoCrNi coatings. The main phases of the Ni55 coating contained  $\gamma\text{-Ni}$ , CrB,  $M_{23}C_6$ ,  $M_3C_2$ ,  $\text{Fe}_3\text{C}$ , and  $\text{Ni}_3\text{Si}$ , while the CoCrNi coating had a single-phase FCC solid solution structure. Figure 2 shows the cross-sectional SEM images of the two specimens. The main component distribution mapping of the two coatings is shown in Fig. 3, and the chemical composition of the marked regions is listed in Table 3. EDS analysis of the Ni55 coating revealed that the  $\gamma\text{-Ni}$  matrix consisted of a large amount of Ni and Cr and a low quantity of Cu, Fe, Si, and C elements. High amounts of Cr and C elements were detected in the Carbide. The CrB contained Cr and B elements, as well as small amounts of other elements, which was consistent with the previous report [34]. In the MEA coating, the grey region was the CoCrNi matrix, which composed of Co, Cr, and Ni with similar atomic ratios. The dark phase were the oxides of Co, Cr and Ni.

The thickness of Ni55 coating and CoCrNi coating was respectively  $612 \pm 20 \mu\text{m}$  and  $620 \pm 21 \mu\text{m}$ . Both coatings had high densities, and no apparent pores or cracks were found. The Ni55 coating contained more precipitated phases, resulting in an uneven distribution of Ni, Cu, and Fe elements. The elements in the CoCrNi coating were evenly distributed without significant component segregation, which contributed to enhancing the corrosion resistance of the coating. Because of the diffusion heat treatment after spraying, there was a diffusion layer between the coating and the substrate, forming a metallurgical bond, which could improve the bonding force between the coating and the substrate [35]. The width of the diffusion layer of the Ni55 coating was approximately 50  $\mu\text{m}$ . The main elements of the diffusion layer were Ni, Cu, and Fe. This was because Ni, Cu, and Fe could be dissolved in each other to generate a solid solution. The width of the diffusion layer of the CoCrNi coating was approximately 10  $\mu\text{m}$ , and the main elements of the diffusion layer were Ni and Cu.

**Table 1** Process parameters for gas-atomized CrCoNi and Ni55 powder

Heating power (kW)	Pouring temperature (°C)	Nozzle diameter (mm)	Atomization pressure (MPa)	Atomization time (s)	Atomizing gas (purity: 99.99%)
100	1520	4.5	3.2	320	Ar

Combining the SEM images and the EDS analysis results at different locations of the coatings, some carbides in the Ni55 coating were strip-shaped, which were easily identified, as shown in position 2 in Fig. 3a. However, CrB and some carbides were blocky and need to be distinguished by EDS or TEM. For example, position 3 in Fig. 3a was blocky CrB identified by EDS. As the Ni55 powder is self-fluxing, during the spraying process, the B and Si elements contained in it had the slag-forming ability, and the formed protective slag could prevent the coating from being oxidized [36]. Therefore, no apparent oxides were found in the Ni55 coating. A small amount of the CoCrNi powder was oxidized during the spraying process to form metal oxides, as shown in the black area in Fig. 3b. The oxidation of the CoCrNi MEA was inhibited in two ways, one was to reduce the oxygen-to-fuel ratio, thus diminishing the oxidizability of the flame. The second was to reduce the spraying distance to shorten the exposure time of metal powder. Note that the peaks associated with the oxides in the CoCrNi coatings were not observed in the XRD pattern because the phase with small content was difficult to be detected by XRD. The TEM images of the two coatings are given in Fig. 4. In addition to the CrB and  $M_{23}C_6$  precipitates, there was also bulk  $Ni_3Si$  with a size of only tens of nanometers in the Ni55 coating. Twins were observed in the CoCrNi coating, as shown in Fig. 4c. The formation of the twins was related to the low stacking fault energy of CoCrNi MEA and the thermomechanical treatment during the HVOF process.

The EBSD results of the Ni55 and CoCrNi coatings parallel to the spraying direction are shown in Fig. 5. The grain growth of the two coatings had no obvious preferred orientation, and the grain size distribution was not uniform. The morphology and size of the crystal grains depend on the manufacturing process. During the HVOF spraying process, the temperature field was not uniformly distributed, and the powder was not completely melted. This promoted the formation of crystal grains with a large size span in the coating [37]. Figure 5a<sub>2</sub> displays the phase distribution in the Ni55

coating. The blue color is the  $\gamma$ -Ni matrix, the red color is CrB, and the green color is  $Fe_3C$ . Owing to the limitations of the EBSD test, the diffraction of different phases interfered with each other, resulting in the failure to identify the phases in some areas, which were marked in black in Fig. 5a<sub>2</sub>. Figure 5a<sub>3</sub> shows the phase boundary distribution of the Ni55 coating. The volume percentages of  $\gamma$ -Ni, CrB, and  $Fe_3C$  were 52.6%, 23.2%, and 2.66%, respectively. Figure 5a<sub>4</sub>, b<sub>2</sub> show the GB distribution of the Ni55 and CoCrNi coatings, respectively. In the Ni55 coating, the average grain sizes of  $\gamma$ -Ni, CrB, and  $Fe_3C$  were 0.97  $\mu m$ , 0.59  $\mu m$ , and 0.47  $\mu m$ , respectively, while the average grain size of the MEA coating was 2.02  $\mu m$  (Fig. 6).

In the field of grain boundary (GB) engineering research, the optimization of GB control and design was achieved by increasing the ratio of low coincidence site lattice (CSL) GBs [38]. Usually,  $\Sigma$  represents the proportion of coincident lattices on the GB. GBs with  $\Sigma \leq 29$  are called low  $\Sigma$ CSL GBs, and other GBs with orientation angle  $\theta > 15^\circ$  are defined as random high-angle boundaries (RHABs). The orientation difference between annealing twins and matrix grains is  $< 111 > / 60^\circ$ , corresponding to  $\Sigma 3$  grain boundary in CSL model [39]. Studies have shown that increasing the proportion of low  $\Sigma$ CSL GBs, particularly the proportion of  $\Sigma 3$  twin boundaries and their geometrically related  $\Sigma 9$  and  $\Sigma 27$  high-order grain boundaries, could significantly improve the corrosion resistance [40]. The GB characteristics of the two coatings are listed in Table 4. The proportions of the low  $\Sigma$ CSL GBs of the Ni55 and CoCrNi coatings were 2.68% and 9.34%, respectively.

Usually, after the material is fabricated, the traditional thermomechanical process of rolling + annealing is used to increase the low  $\Sigma$ CSL GB ratio [41, 42]. However, in this study, no extra deformation treatment was used. Still, a high proportion of the low  $\Sigma$ CSL GBs was obtained in the CoCrNi coating, which was closely related to the material properties and the process characteristics of HVOF. The CoCrNi MEA were subjected to strong thermo-mechanically coupled effects during the HVOF process, the large strain and high strain rate normally result in the grain boundaries evolution. The stacking fault energy of the CoCrNi MEA was only  $22 \pm 4 \text{ mJ m}^{-2}$ , which was lower than that of austenitic stainless steel and the typical CoCrFeMnNi HEA [23]. The high  $\Sigma$ CSL GBs in low to medium stacking fault energy FCC metal materials with deformation will decompose to form  $\Sigma 3$  GBs and other low  $\Sigma$ CSL GBs during the high-temperature annealing process [43]. Moreover, the development

**Table 2** Chemical compositions of the Ni55 and CoCrNi powders (wt%)

Powder	C	Mo	Cu	Fe	Cr	Si	B	Co	Ni
Ni55	0.5	3	3	2.5	16	4	3.5	–	67.5
CoCrNi	–	–	–	–	29.6	–	–	33.9	36.5

**Fig. 1** X-ray diffraction profiles of **a** Ni55 coating and **b** CoCrNi coating

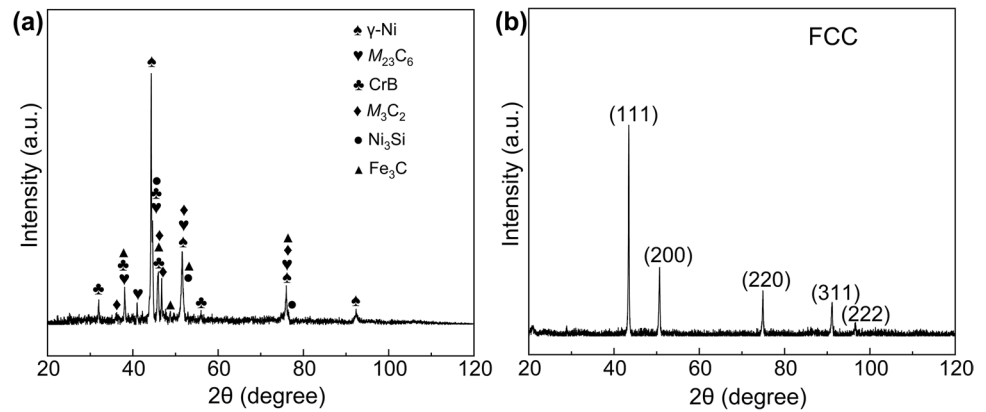
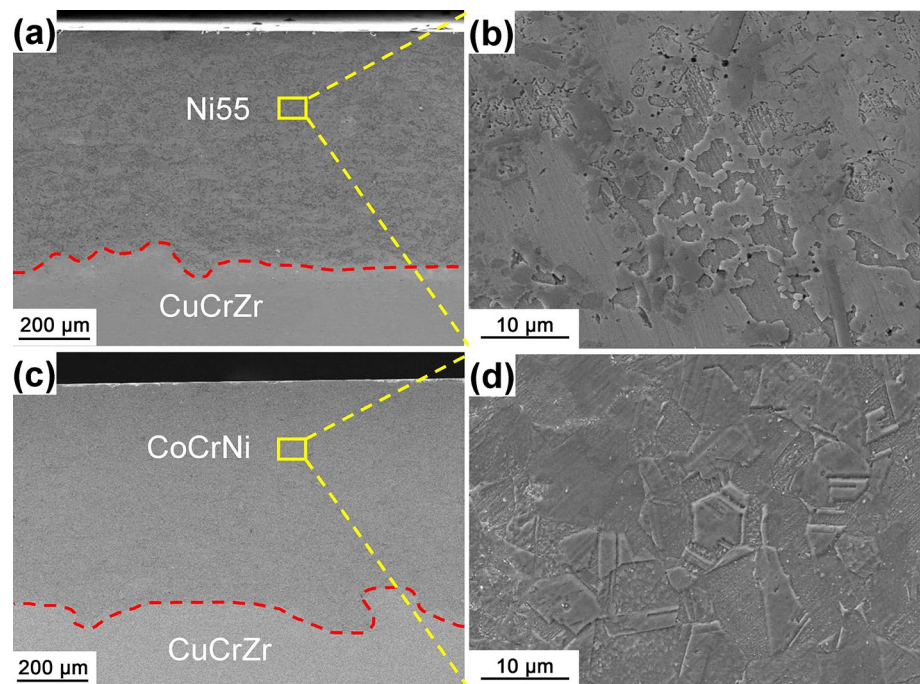


**Fig. 2** Cross-sectional SEM images of the **(a, b)** Ni55 and **(c, d)** CoCrNi coatings



trend of the HVOF spraying system is to continuously reduce the temperature of particles and increase their flight speed. The spray-type combustion chamber of the HVOF spraying system has a pressure of up to 1 MPa, which can accelerate the particles to more than 600 m/s, and only small particles and some large particles are melted before they hit the substrate [44]. During the impact of molten and semi-molten particles on the substrate, significant shot peening stress occurs, resulting in plastic deformation. The finite element model predicted that when the 316 stainless steel particles flew at 520 and 610 m/s, the impact stress of the particles on the coating was as high as 156 and 277 MPa, respectively [45]. Furthermore, the yield strength of the rolled CoCrNi MEA was 438 MPa at 25 °C, and its strength decreased with increasing temperature [25]. Such an immense impact stress was sufficient to cause plastic deformation. Therefore, the CoCrNi coating contained a large amount of low  $\Sigma$ CSL GBs.

### 3.2 Electrochemical Corrosion Behavior in NaF Solution

The corrosion resistance of the Ni55 and CoCrNi coatings in the NaF solution was evaluated by the potentiodynamic polarization and EIS experiments. Prior to commencing the polarization test, the OCP was stabilized for 1 h. Figure 7a shows the variation curves of the OCP of the CuCrZr substrate and the two coatings with time. At the initial stage of the test, the OCP of the CuCrZr decreased instantaneously. This negative potential movement was related to the removal of the oxide film on the alloy surface. The surface of the CuCrZr was covered with a natural oxide film before immersion. When immersed in NaF solution,  $F^-$  broke down the oxide film and eroded the alloy surface. At this time, the OCP decreased significantly. When the protection of the corrosion product film and the erosion effect of  $F^-$  reached

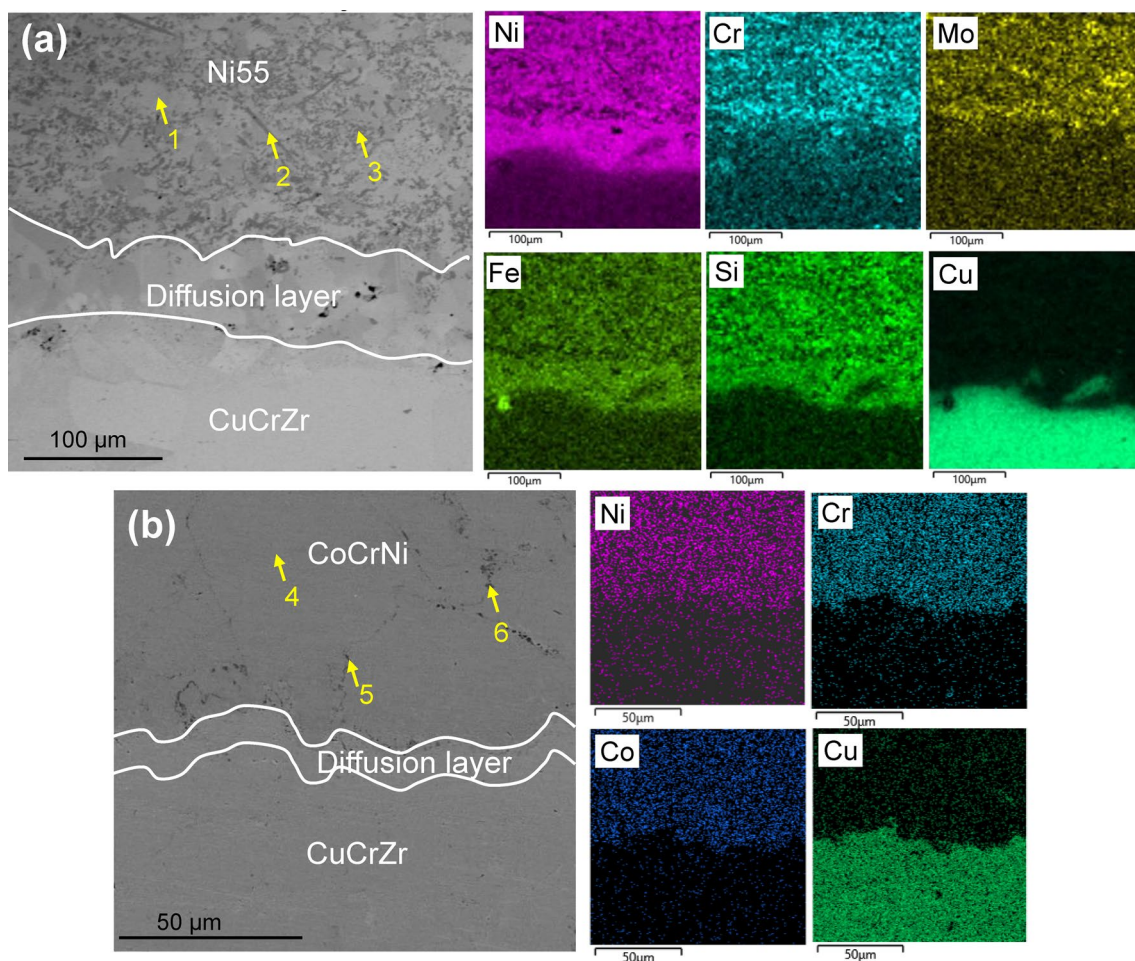


**Fig. 3** EDS mapping of **a** Ni55 and **b** CoCrNi specimens

**Table 3** Chemical composition of the marked regions in the Ni55 and CoCrNi coatings (wt%)

Samples	Point	Phase	Ni	Cr	Co	Cu	Fe	Mo	Si	B	C	O
Ni55	1	$\gamma$ -Ni	76.18	12.78	–	3.6	3.24	0.61	3.13	–	0.46	–
	2	Carbide	2.28	68.31	–	0.84	0.96	4.78	0.12	0	22.71	–
	3	CrB	2.84	74.18	–	1.15	0.13	2.34	0.16	17.26	1.94	–
CoCrNi	4	CoCrNi	34.38	33.04	32.58	–	–	–	–	–	–	–
	5	Oxide	13.93	27.87	15.46	–	–	–	–	–	–	42.74
	6	Oxide	23.54	26.81	23.45	–	–	–	–	–	–	26.19

dynamic equilibrium, the OPC tended to be stable. Different from the CuCrZr substrate, the OCPs of the two coatings gradually increased and tended to be stable with the extension of time. Overall, the OCP of the CoCrNi MEA was higher than that of the Ni55 and CuCrZr, revealing that the CoCrNi MEA exhibited a more ‘noble’ OCP [46]. In addition, potential fluctuations were observed on the OCP curves of the two coatings, which could be explained by the instantaneous competition between the growth and dissolution of the passive film on the electrode surface [47]. That

is, the passive film in the fluctuating region in the corrosive medium was still unstable, and the micro defects of the passive film caused the potential to decrease. Subsequently, rapid re-passivation of the damaged passive film led to an increase in potential, and this process was repeated, causing potential fluctuations.

Figure 7b shows the potentiodynamic polarization curves of the two coatings in the NaF solution. The polarization curves of the two coatings exhibited a significant activation-passivation transition, and the passivation current density

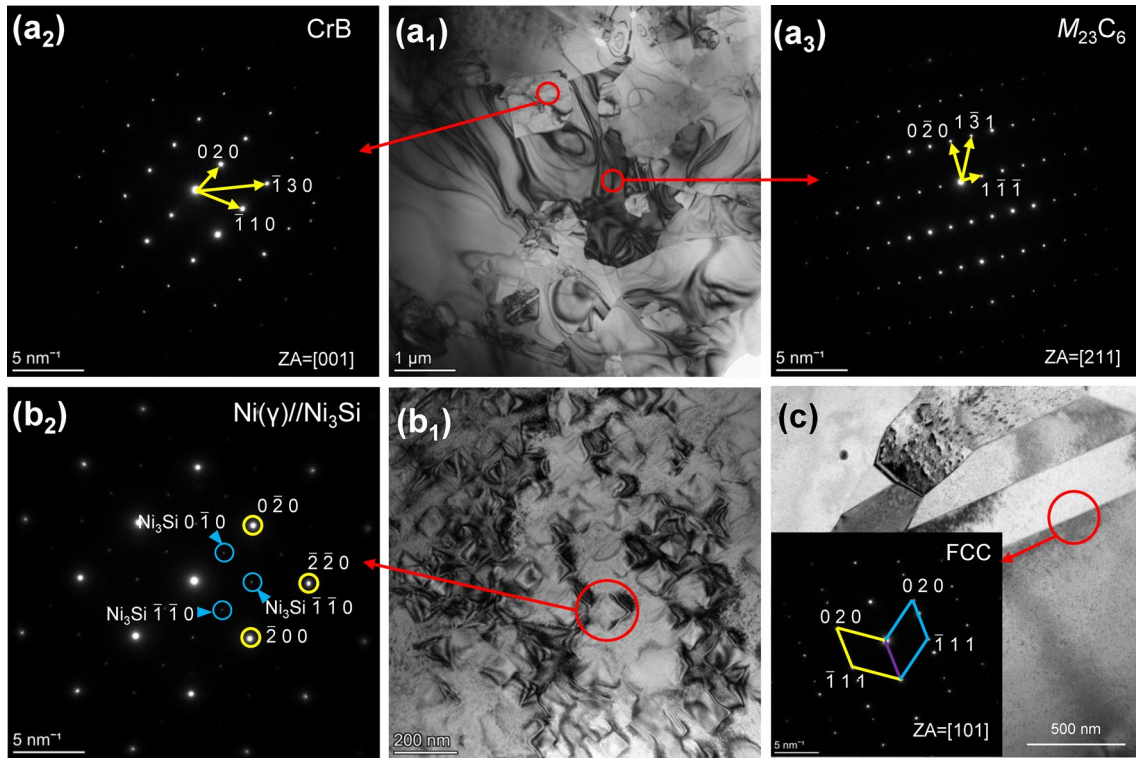


Fig. 4 TEM images and the associated selected diffraction spots of (a<sub>1</sub>–a<sub>3</sub>, b<sub>1</sub>–b<sub>2</sub>) Ni55 coating and c CoCrNi coating

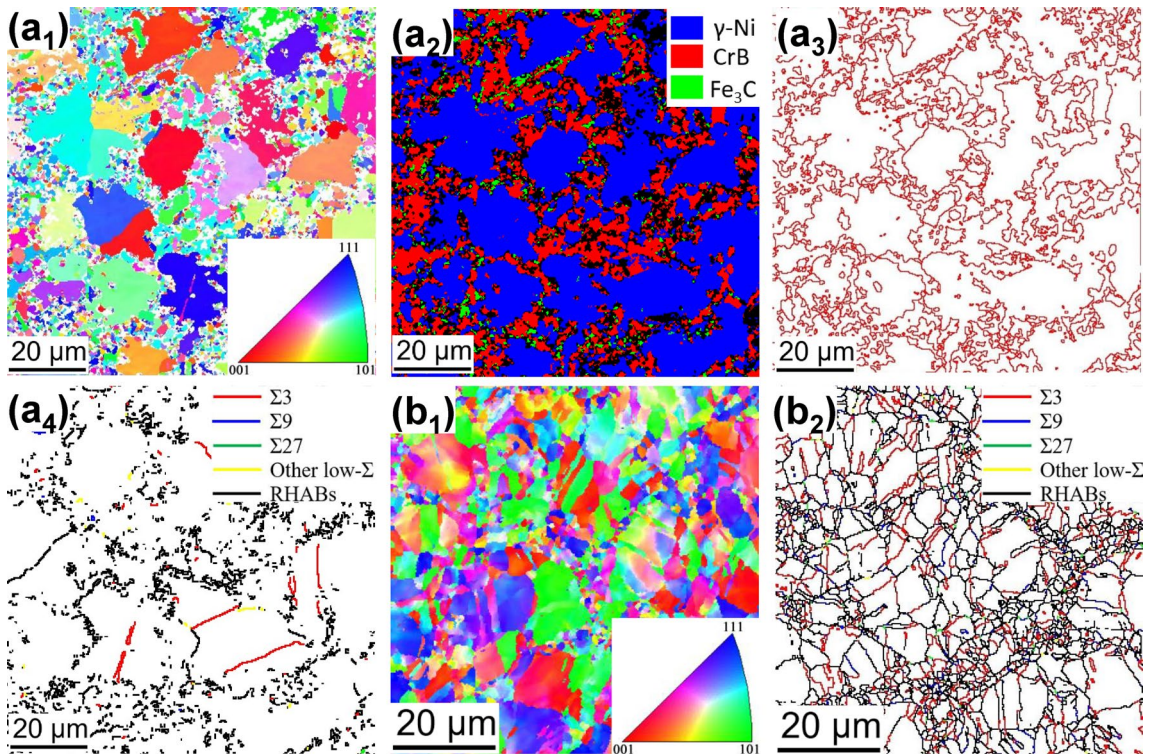


Fig. 5 EBSD results of the coating parallel to the spraying direction. (a<sub>1</sub>, b<sub>1</sub>) EBSD inverse pole diagram; (a<sub>2</sub>) phase distribution; (a<sub>3</sub>) phase boundary distribution; (a<sub>4</sub>, b<sub>2</sub>) grain boundary characteristic distribution. (a<sub>1</sub>–a<sub>4</sub>) Ni55 coating, (b<sub>1</sub>–b<sub>2</sub>) CoCrNi coating

of the Ni55 coating was significantly higher than that of the CoCrNi coating. Only one anode/cathode transition was observed in the CrCoNi coating, while two transition peaks were observed in the Ni55 coating. Annica [48] believed this was a sign of electrochemical activity on or within the oxide film. This was related to the multiphase microstructure of the Ni55 coating. The corrosion potential ( $E_{\text{corr}}$ ), corrosion current density ( $i_{\text{corr}}$ ), and polarization resistance ( $R_p$ ) values are summarized in Table 5. The two coatings showed smaller  $i_{\text{corr}}$ , higher  $R_p$ , and a broader passivation region than that of the CuCrZr substrate, revealing the lower corrosion tendency of the coatings. Compared with the Ni55 coating, the  $i_{\text{corr}}$  of the CoCrNi coating was reduced by 78.8%, and the polarization resistance was increased by 7.13 times, which implied that the CoCrNi coating had better corrosion resistance in the NaF solution.

Figure 8 shows the EIS test results of the coatings in the NaF solution under OCP conditions. The Nyquist diagrams of the two coatings exhibited an incomplete semicircular shape (Fig. 8a), implying that the corrosion process was mainly controlled by charge transfer. The larger the radius of the capacitor arc in the Nyquist diagram, the more stable the passive film on the surface, and the higher the corrosion resistance of the sample [49]. The radius of the capacitor arc of the CoCrNi coating was significantly more extensive than that of the Ni55 coating, which revealed that the CoCrNi coating owned superior corrosion resistance. The CoCrNi coating has a relatively high phase angle (Fig. 8b) and large impedance modulus (Fig. 8c).

**Table 4** Grain boundary characteristic distribution statistics of as-build and annealed HEA

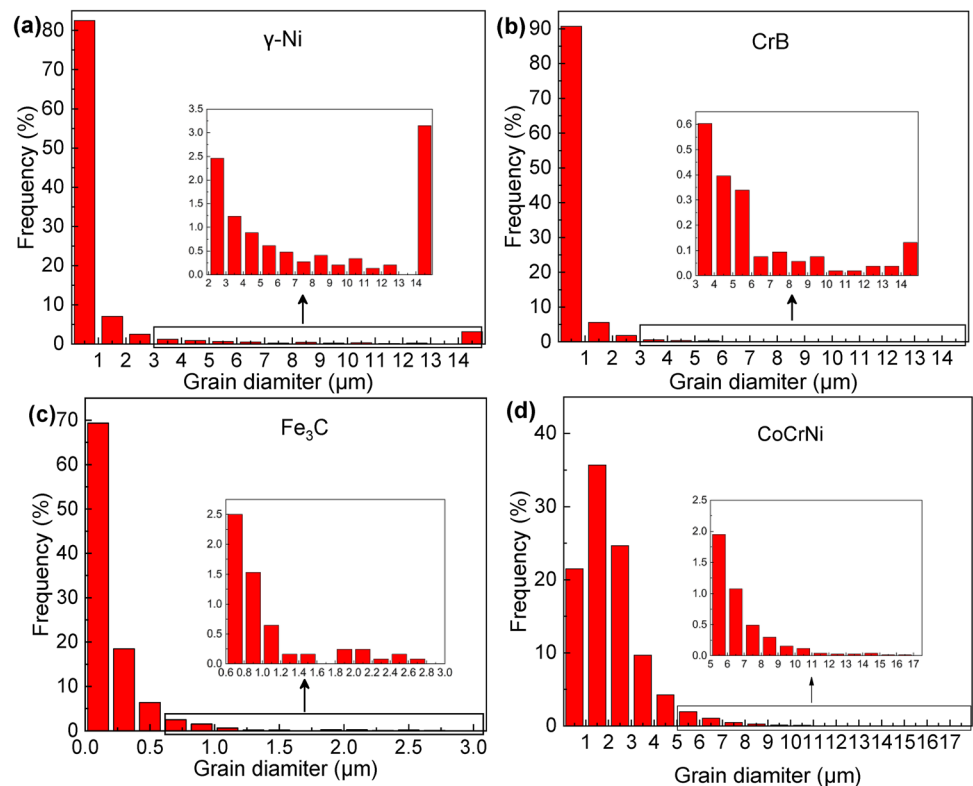
Samples	$\Sigma 3$ (%)	$\Sigma 9 + \Sigma 27$ (%)	Other low $\Sigma$ CSL (%)	Overall low $\Sigma$ CSL ( $\Sigma \leq 29$ ) (%)
Ni55	2.36	0.30	0.02	2.68
MEA	7.34	0.41	1.59	9.34

Furthermore, the value of the  $|Z|$  at a fixed frequency of 0.1 Hz is usually related to the polarization resistance  $R_p$  of the coating. A more enormous  $|Z|$  value indicates the better corrosion resistance of the alloy [50]. At 0.1 Hz, the  $|Z|$  value of the CoCrNi MEA was higher than that of the Ni55, which also proved that the CoCrNi coating had excellent corrosion resistance.

To quantitatively analyze the impedance response of the passive film of the coating in the NaF solution, the EIS experimental data were fitted using the electrical equivalent circuit (EEC) model in Fig. 8d. Considering the non-ideal capacitance behavior of the metal/solution interface, the EEC contains constant phase elements (CPE). And the impedance of the CPE was calculated by the following equation [51, 52]:

$$Z_{\text{CPE}} = \frac{1}{Q}(j\omega)^{-n} \quad (1)$$

**Fig. 6** The grain size distribution diagram of **a**  $\gamma$ -Ni, **b** CrB, and **c**  $\text{Fe}_3\text{C}$  in the Ni55 coating, **d** CoCrNi coating





where  $Q$  is the admittance of the CPE,  $\omega$  is the angular frequency, and  $n$  is the exponent of the CPE ( $0 \leq n \leq 1$ ). When  $n=0$ , CPE means pure resistance  $Z=R$ ; when  $n=1$ , CPE represents pure capacitance  $Z=C$ ; when  $n=0.5$ , CPE is Warburg impedance  $Z=W$ .

The EEC comprises a solution resistance ( $R_s$ ), in series with two  $R$ -CPE elements [48, 53, 54]. The high-frequency time constant  $R_f(\text{CPE}_1)$  is related to the area covered by the passive film and is represented by the passive film admittance  $\text{CPE}_1$  and the passive film resistance  $R_f$ . The low-frequency time constant  $R_{ct}(\text{CPE}_2)$  is assigned to the active area with weak passivation film or surface defect, and is represented by the charge transfer resistance  $R_{ct}$  and the admittance  $\text{CPE}_2$ . These active areas were more likely to be broken by fluoride ions and thus corroded. Table 6 shows the EEC fitting parameters of the two coatings under the OCP conditions. The value of the CPE and its coefficient  $n$  is related to the heterogeneity of the electrode surface, and the value of  $n$  indicates the deviation from purely capacitive behavior [52]. The coefficient  $n_1$  of  $\text{CPE}_1$  was lower than 1, revealing that the heterogeneous passivation film was formed on the coating [55]. Similarly,  $n_2$  less than 1 indicated that the active area was eroded by fluoride ions to form a surface with heterogeneities (roughness and surface defects) [50]. The charge transfer resistance  $R_{ct}$  values of both coatings were significantly lower than their  $R_f$  values, which demonstrated the passivation film in the active area was weak or absent [56]. In addition, the higher  $R_{ct}$  of the CoCrNi coating confirmed that the passive film of the CoCrNi coating was relatively intact and that charge transfer was more difficult [54]. Therefore, the MEA coating has better resistance to NaF solution than the Ni55 coating, consistent with the results of the potentiodynamic polarization test.

### 3.3 Characteristics of the Passive Films

The composition of the passive film directly affects the corrosion resistance of the material. Therefore, the composition

of the passive film formed on the coating in the NaF solution was analyzed using XPS. Figures 9 and 10 show the fitting results of the XPS data of the Co 2p<sub>3/2</sub>, Cr 2p<sub>3/2</sub>, Ni 2p<sub>3/2</sub>, Fe 2p<sub>3/2</sub>, Cu 2p<sub>3/2</sub>, Mo 3d, and O 1 s in the passive film on the coatings after passivation for 1 h at +400 mV<sub>SCE</sub>. The dots represent the experimental data, and the solid line is the fitting curve. The parameters for fitting the XPS spectra are shown in Table 7. During the XPS peak fitting, the peak position values of the compounds were referred to in the previous literature, and the peak positions of the same compounds were not exactly the same [57, 58]. The results showed that the components of the passive film were mainly metal oxides and hydroxides.

The atomic fraction ( $C_x$ ) of each component in the passive film was obtained from the formula [59]:

$$C_x = \frac{I_x/S_x}{\sum I_i/S_i} \quad (2)$$

where  $I_x$  is the peak area of each element, and  $S_x$  is the atomic sensitivity factor. The statistical results of various components in the passive film are shown in Fig. 11. Cr oxides and hydroxides play the most critical role in improving the corrosion resistance of materials. For example, Cr<sub>2</sub>O<sub>3</sub> with a dense structure could maintain excellent stability over a wide pH range (2–12), which significantly improved the protective ability of the passive film [55, 60]. Increasing Ni content is beneficial to enhance corrosion resistance. Moreover, the enrichment of Ni in the metal state at the metal/oxide interface also reduced the dissolution rate of the oxide

**Table 5** Polarization curve data of CuCrZr substrate, Ni55 and CoCrNi coatings in 3.5 wt% NaF solution

Samples	$i_{\text{corr}}$ ( $\mu\text{A cm}^{-2}$ )	$E_{\text{corr}}$ (V <sub>SCE</sub> )	$R_p$ ( $\Omega \text{ cm}^2$ )
CuCrZr	$11.2 \pm 0.09$	$-0.392 \pm 0.031$	$2664 \pm 156$
Ni55	$8.72 \pm 0.85$	$-0.754 \pm 0.065$	$3481 \pm 312$
CoCrNi	$1.85 \pm 0.14$	$-0.648 \pm 0.029$	$28,299 \pm 2337$

**Fig. 7** **a** Open-circuit potential and **b** potentiodynamic polarization curves of CuCrZr substrate, Ni55 and CoCrNi coatings in 3.5 wt% NaF solution

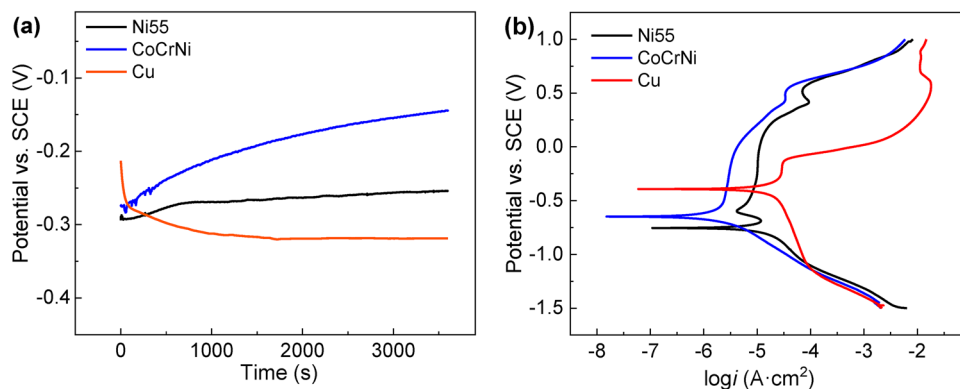
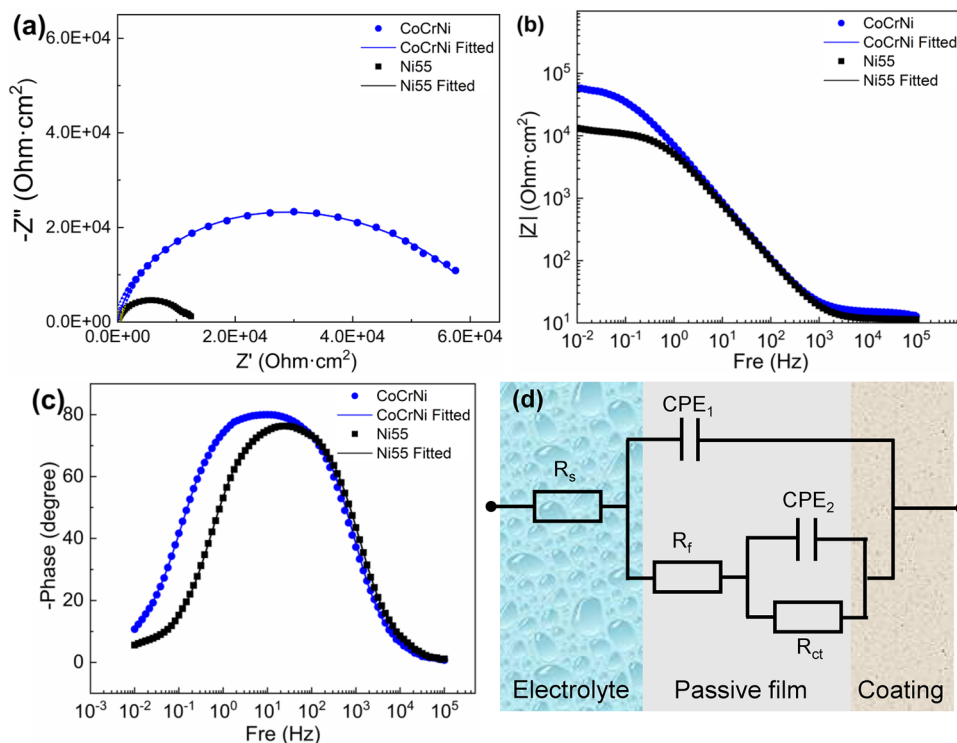


**Fig. 8** EIS plots of the coatings in 3.5 wt% NaF solution. **a** Nyquist plots; **(b, c)** Bode plots; **d** the corresponding equivalent circuit model



[61]. Yang et al. [20] argued that adding Cu significantly improved the corrosion resistance of the Ni60 coatings. The  $\text{Cr}_2\text{O}_3$ , NiO, and CuO in the passive film isolated the coating from the corrosion medium, effectively slowing down the seepage damage of the coating by the corrosion ions, thereby reducing the corrosion rate. The effect of Mo on the corrosion behavior was simultaneous to its content and the corrosion solution, which still needs to be studied in depth [62]. Moreover, Shang et al. [63] pointed out that the compactness of the oxides of each element was arranged in the order of  $\text{Cr}_2\text{O}_3 > \text{NiO} > \text{CoO} > \text{FeO}$ . Therefore, it is believed that the Cr, Ni, and Cu in the coating played a protective role in the passive film. The higher the total proportion of Cr, Cu, and Ni in the passive film, the stronger the corrosion resistance of the coating. Through calculation, the real ratios of Cr, Cu, and Ni in the Ni55 and MEA coatings were 70.9% and 80.5%, respectively. This indicates that the MEA coating has a more protective passive film in the NaF solution.

### 3.4 Morphology of Corroded Surfaces

To study the immersion corrosion behavior of the two coatings, the specimens were immersed in the NaF solution for 7 days at room temperature. Figure 12 illustrates the corroded surface morphology and height variations of the coatings. In contrast, the Ni55 coating had a ‘rougher’ surface with localized corrosion manifestation. The depth of the localized corrosion site was between 1–2  $\mu\text{m}$ , and the average roughness of the corroded surface was 0.53  $\mu\text{m}$ . The

corrosion type of the CoCrNi coating was mainly uniform corrosion without any visible localized corrosion penetrating into the coating, and the corrosion surface is smoother (average roughness is 0.19  $\mu\text{m}$ ). A large amount of corrosion products was covered on the corroded surface of the two coatings. The number of corrosion products of Ni55 coating was higher than that of CoCrNi coating, and the size was more significant.

EDS analysis of the marked regions on the corroded surfaces was conducted, and the results are given in Fig. 13 and Table 8. The corrosion of the Ni55 coating mainly occurred in the Cr-poor region around the Cr-rich precipitated phase, and the Cr-rich precipitated phases were almost uncorroded. Besides, the  $\gamma$ -Ni substrate with high content of Ni and Cu was not easily corroded. This confirms that  $\text{Cr}_2\text{O}_3$ , CuO, and NiO in the passive film could isolate the coating from the corrosive medium and effectively protect the coating from deep erosion. These areas were transformed into oxide films and protected the alloy from obvious attacks. Furthermore, Chang et al. [64] found that preferential corrosion also occurred at the phase boundary between the  $\text{Ni}_3\text{Si}$  particles and the  $\gamma$ -Ni solid solution. After the CoCrNi coating was eroded, the constituent elements were still evenly distributed. The corrosion products of the two coatings were mainly complexes consisting of metal oxides and fluorides.

Figure 14 presents a schematic diagram of the corrosion process of the two coatings. Firstly, a stable passive film was first generated on the coating surface in the NaF solution. In the early stage of corrosion, cracks occurred at the weak

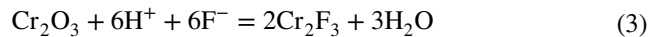
**Table 6** Equivalent circuit fitting parameters for EIS of Ni55 and CoCrNi coatings in 3.5 wt% NaF solution under OCP conditions

Samples	$R_s/\Omega \text{ cm}^2$	$\text{CPE}_1/\Omega^{-1} \text{ s}^n \text{ cm}^{-2}$	$n_1$	$R_f/\Omega \text{ cm}^2$	$\text{CPE}_2/\Omega^{-1} \text{ s}^n \text{ cm}^{-2}$	$n_2$	$R_{ct}/\Omega \text{ cm}^2$
Ni55	11.4	$3.15 \times 10^{-5}$	0.889	$1.09 \times 10^4$	$1.39 \times 10^{-3}$	0.676	$3.04 \times 10^3$
CoCrNi	14.8	$2.75 \times 10^{-5}$	0.904	$5.16 \times 10^4$	$3.78 \times 10^{-4}$	0.796	$1.12 \times 10^4$

points or areas of the passive film. For the Ni55 coating, galvanic corrosion was formed between different phases, and corrosion first occurred at the phase boundary. At this time, the corrosive solution caused the active dissolution of the anode. Besides, on account of their high energy and high diffusivity, RHABs often become the growth core and propagation channel of corrosion cracks [38]. Subsequently, the corrosion dissolution expanded into the grain interior, resulting in further erosion of the coating. On account of the uniformity of the microstructure of the CoCrNi coating, a more protective and uniform passive film was formed. Moreover, the proportion of the low  $\Sigma$ CSL GBs in the CoCrNi coating was relatively high, which can break the connectivity of the RHAB network and effectively inhibit intergranular corrosion. Therefore, the CoCrNi coating underwent uniform corrosion.

The corrosion products of the Ni-based alloy and the CoCrNi MEA in the  $\text{Cl}^-$  medium were mainly metal oxides [29, 65, 66]. In contrast, the corrosion products of the two coatings in the NaF solution in this study contained fluorine, which was related to the characteristics of fluorine. In the

early stage of corrosion, F ions could react with the passive film, for example, with  $\text{Cr}_2\text{O}_3$ , according to the following formula [33]:



After the passive film was dissolved, the coating substrate was exposed to the corrosion solution, and the F ions continued to react with the metal elements in the coating [67]:



In the formula,  $\text{Me}$  represents elements such as Ni, Mo, Fe, Cr, and Cu. The first-principles simulation study found that the adsorption energy of Cr (3.52 eV) on F was higher than that of Ni(111) surface (2.48 eV). Cr becomes a trap site for F atoms, and the diffusion of F atoms from the vicinity of the Ni(111) surface to the Cr site was a process without energy barriers [68]. The diffusion and adsorption of F atoms promoted the formation of strong F-Cr bonds. The Cr-Ni bond was elongated and weakened, which significantly affected the dissolution of Cr-Ni. Ren et al. [33]

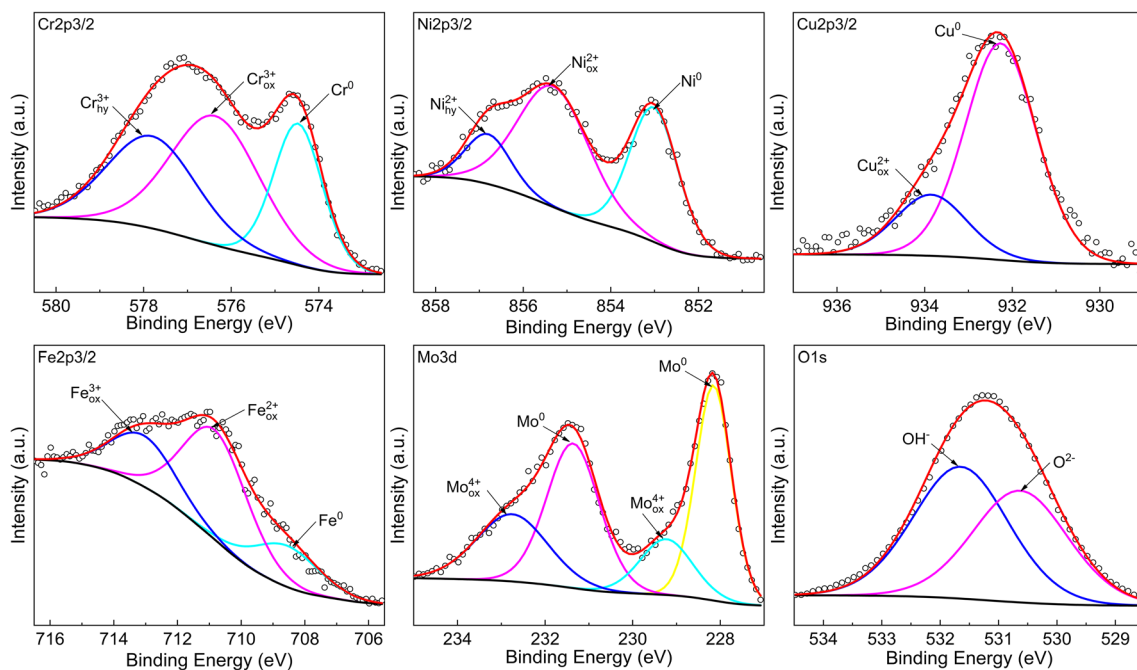


**Fig. 9** XPS high-resolution spectra obtained from the passive films formed on the Ni55 coating after passivation for 1 h at +400 mV<sub>SCE</sub> in 3.5 wt% NaF solution

**Fig. 10** XPS high-resolution spectra obtained from the passive films formed on the CoCrNi coating after passivation for 1 h at +400 mV<sub>SCE</sub> in 3.5 wt% NaF solution

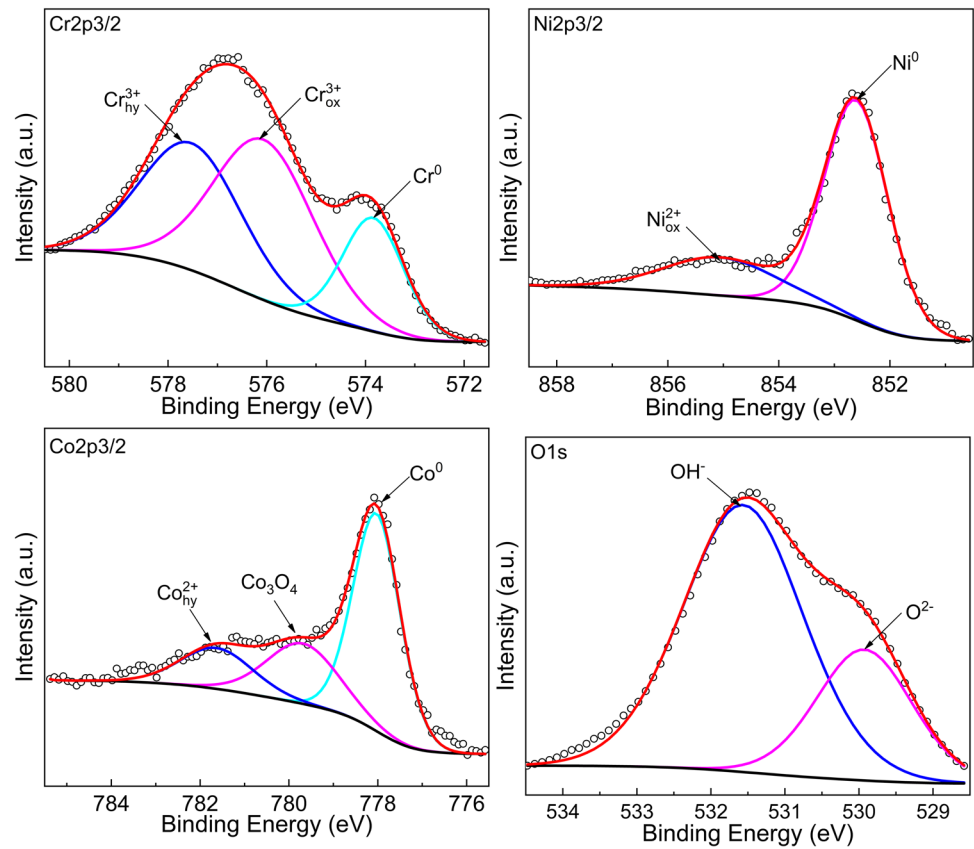


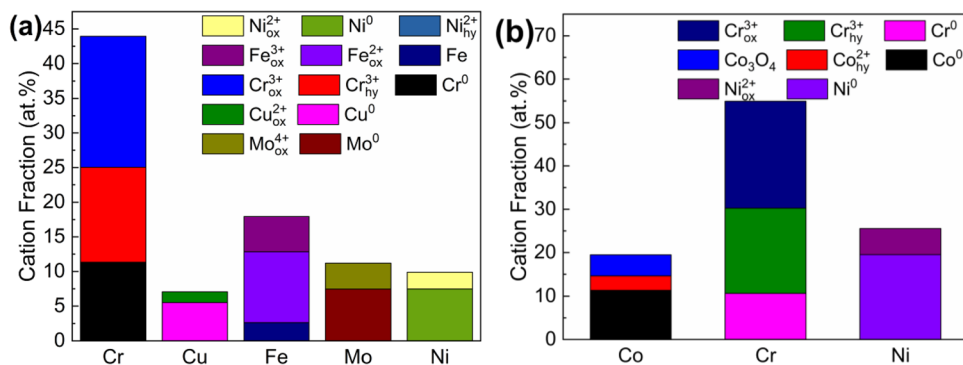
**Table 7** The parameters for fitting the XPS spectra: binding energy (BE), FWHM value and area

Sample	Composition	BE (eV)	FWHM (eV)	Area (CPS eV)	Sample	Composition	BE (eV)	FWHM (eV)	Area (CPS eV)	
Ni55	Cr <sup>3+</sup> <sub>ox</sub>	576.4	2.4	37,120	CoCrNi	Co <sup>0</sup>	778.0	1.25	37,435	
	Cr <sup>0</sup>	574.5	1.32	22,297		Co <sub>3</sub> O <sub>4</sub>	779.7	1.92	15,956	
	Cr <sup>3+</sup> <sub>hy</sub>	577.8	2.4	26,454		Co <sup>2+</sup> <sub>hy</sub>	781.6	1.92	10,806	
	Cu <sup>0</sup>	932.3	1.92	15,462		Cr <sup>3+</sup> <sub>hy</sub>	577.5	2.4	54,533	
	Cu <sup>2+</sup> <sub>ox</sub>	933.9	1.92	4362		Cr <sup>3+</sup> <sub>ox</sub>	576.1	2.4	68,815	
	Fe <sup>0</sup>	708.6	2.5	3045		Cr <sup>0</sup>	573.8	1.46	29,720	
	Fe <sup>2+</sup> <sub>ox</sub>	710.8	2.5	8114		Ni <sup>0</sup>	852.6	1.35	56,611	
	Fe <sup>3+</sup> <sub>ox</sub>	713.1	2.5	6926		Ni <sup>2+</sup> <sub>ox</sub>	855.1	2.4	17,426	
	Mo <sup>0</sup>	228.2	0.96	6668						
	Mo <sup>0</sup> <sub>3/2</sub>	231.4	1.43	6636						
	Mo <sup>4+</sup>	229.2	1.41	2531						
	Mo <sup>4+</sup> <sub>3/2</sub>	232.8	1.92	4162						
	Ni <sup>0</sup>	853.0	1.31	8200						
	Ni <sup>2+</sup> <sub>ox</sub>	855.3	1.92	10,838						
	Ni <sup>2+</sup> <sub>hy</sub>	856.8	1.22	2827						

confirmed that when 316 L stainless steel was immersed in a fluoride-containing solution, F ions entered through the oxide film and preferentially destroyed weak chemical bonds to form complexes with oxide components. For example, F entered and dissolved Fe oxide through the oxide film.

Therefore, the two coatings formed a complex composed of metal oxides and fluorides in the NaF solution.

**Fig. 11** Atomic fraction in the passive film of **a** Ni55 and **b** CoCrNi coatings



### 4 Conclusions

In this paper, the Ni55 and CoCrNi MEA coatings were successfully prepared on the surface of the CuCrZr plates using the HVOF technique. The corrosion behavior and passive film characteristics of the two coatings in a 3.5 wt% NaF solution was compared. The following conclusions are drawn:

1. The CoCrNi coating exhibited superior corrosion resistance in comparison to the Ni55 coating, as well as the CuCrZr substrate. This was attributed to the more uniform composition distribution and a higher proportion of low ΣCSL GBs in the CoCrNi coating.
2. The Ni55 coating was mainly subjected to selective corrosion, and preferential corrosion occurred at the phase boundary between the precipitates and the γ-Ni solid solution. In contrast, the CoCrNi coating was uniformly corroded. The corrosion products of the two coatings in the NaF solution were both complexes composed of metal oxides and fluorides.
3. The passive films of the two coatings were mainly composed of metal oxides and hydroxides. The MEA coating formed a more uniform and protective passive film in the NaF solution; the ratio of Cr + Ni + Cu in the passive film of the MEA coating (80.5%) was higher than that of the Ni55 coating (70.9%). Therefore, the MEA coating showed better corrosion resistance than the Ni55 coating in the NaF solution.

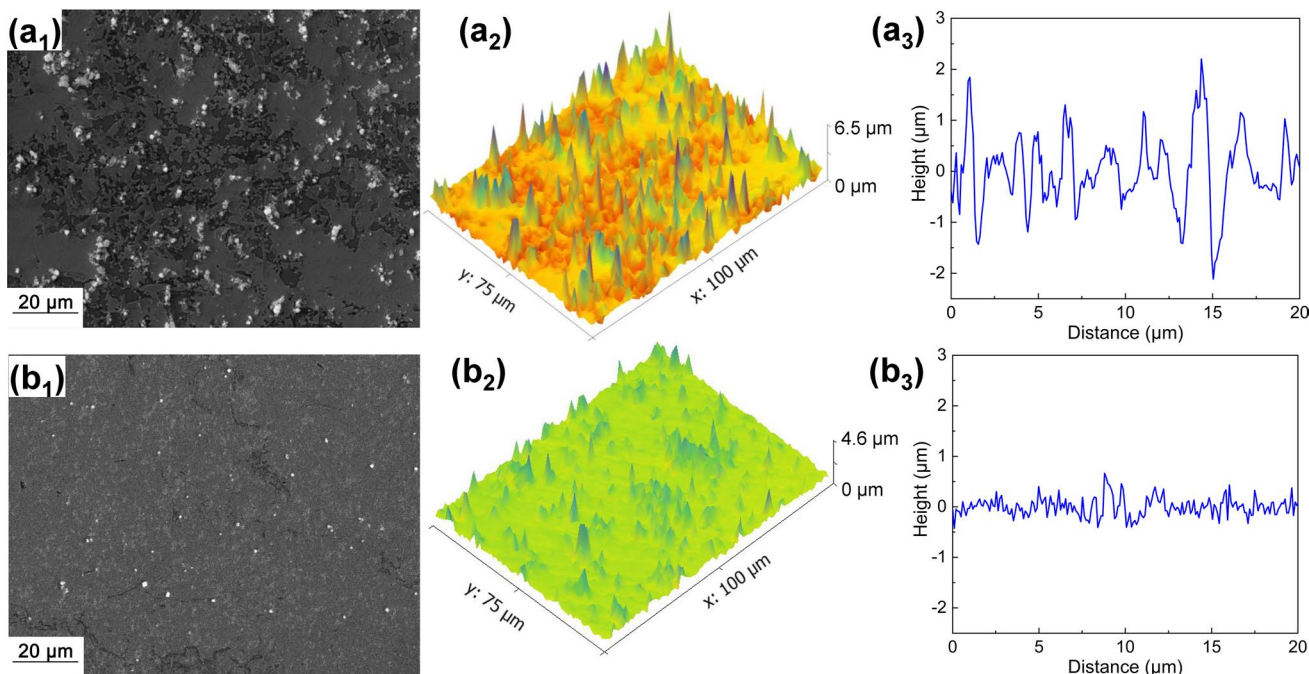


**Fig. 12** (**a<sub>1</sub>**, **b<sub>1</sub>**) SEM images, (**a<sub>2</sub>**, **b<sub>2</sub>**) 3D profiles and (**a<sub>3</sub>**, **b<sub>3</sub>**) height variations of **a** Ni55 and **b** CoCrNi coatings after immersed in 3.5 wt% NaF solution for 7 days

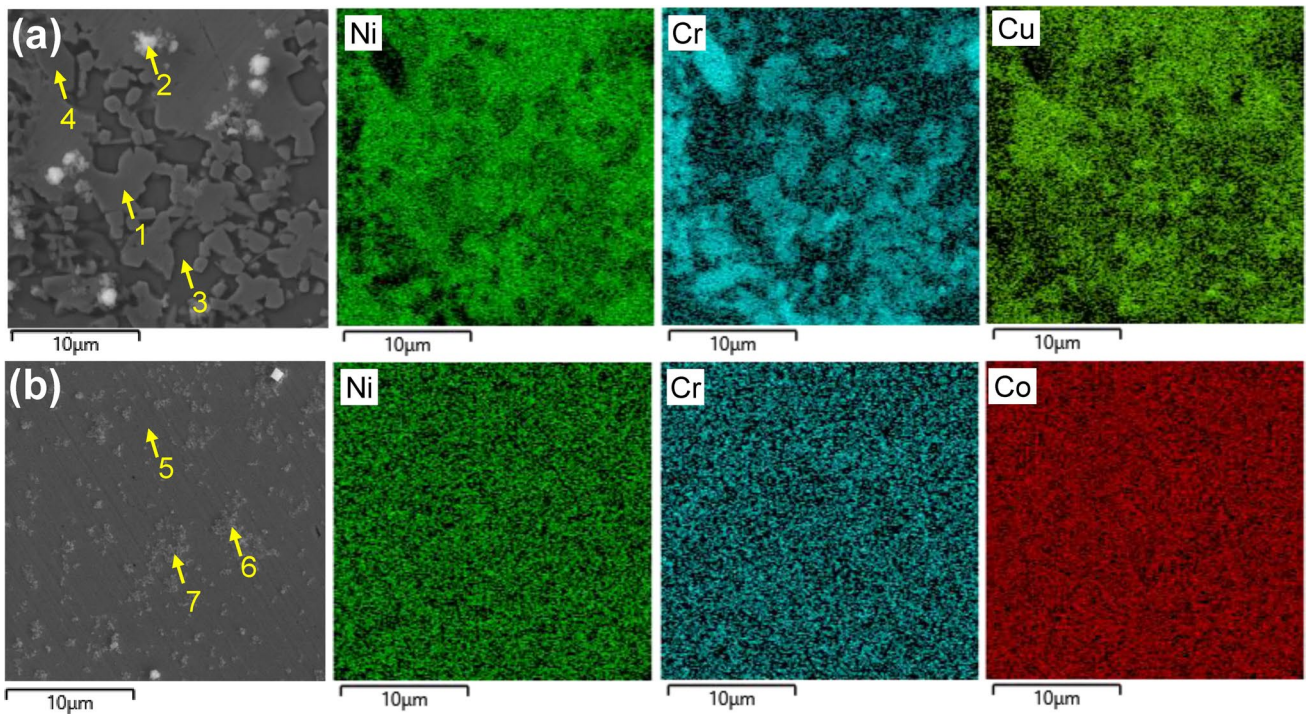


**Fig. 13** EDS results of **a** Ni55 and **b** CoCrNi coatings surface after immersed in 3.5 wt% NaF solution for 7 days

**Fig. 14** Schematic diagram of corrosion process of **a** Ni55 and **b** CoCrNi coatings in 3.5 wt% NaF solution

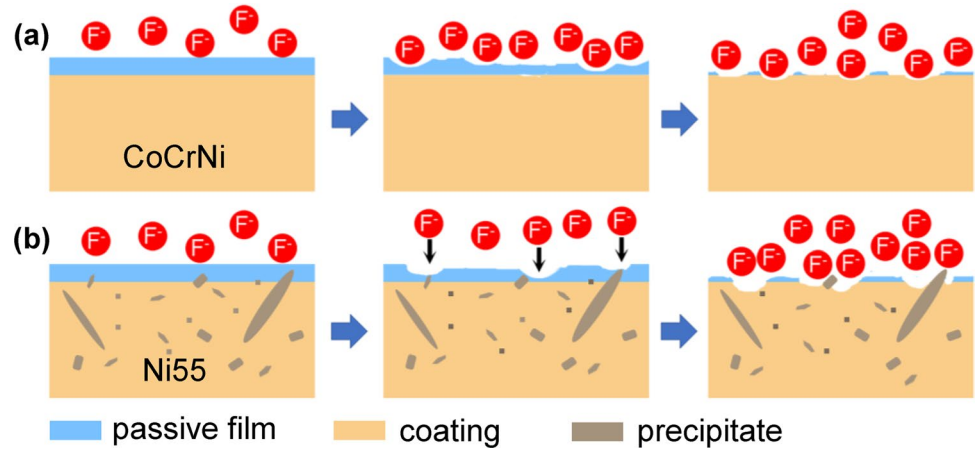


**Table 8** Chemical composition of the typical areas on the corrosion surface of the Ni55 and CoCrNi coatings (wt%)

Coating	Point	Ni	Cr	Co	Cu	Fe	Mo	Si	C	O	F
Ni55	1	40.12	24.06		1.87	0.85	21.38	6.53	0.37	2.94	1.88
	2	47.72	5.96		5.58	4.95	4.42	4.86	1.55	13.51	11.45
	3	70.96	4.38	–	3.8	1.88	0.51	0.8	6	8.31	3.36
	4	2.59	72.1	–	0.28	0.52	4.42	0.2	17.26	1.01	1.62
CoCrNi	5	34.91	30.36	34.18	–	–	–	–	–	0.55	–
	6	30.47	26.56	29.91	–	–	–	–	–	5.15	7.91
	7	33.19	28.39	32.89	–	–	–	–	–	2.58	2.95

**Acknowledgements** This work was supported by the National Natural Science Foundation of China (Grant No. 51971001) and the Key Research and Development Project of Anhui Province (No. 2022a05020017).

## Declarations

**Conflict of interest** The authors declare that they have no conflict of interest.

## References

- H. Zhang, H. Fu, S. Zhu, W. Yong, J. Xie, *Acta Mater.* **215**, 117118 (2021)
- M. Zhang, L. Liu, S. Liang, J. Li, *Met. Mater. Int.* **26**, 1585–1595 (2020)
- A. Pourfathi, R. Tavakoli, *Int. J. Therm. Sci.* **183**, 107860 (2023)
- Y. Liu, T. Xu, Y. Liu, Y. Gao, C. Di, *J. Mater. Res. Technol.* **9**, 8283–8288 (2020)
- S. Barella, A. Gruttadauria, C. Mapelli, D. Mombelli, *Eng. Failure Anal.* **36**, 432–438 (2014)
- J. Srnec Novak, A. Lanzutti, D. Benasciutti, F. De Bona, L. Moro, A. De Luca, *Eng. Failure Anal.* **94**, 480–492 (2018)
- S. Gu, L. Yu, G. Wen, P. Tang, Z. Wang, Z. Gao, *Trans. Indian Inst. Met.* **74**, 775–782 (2021)
- Z. Zhao, J. Zhao, Z. Tan, B. Qu, Y. Cui, *R. Soc. Open Sci.* **7**, 200704 (2020)
- H. Wang, Y. Sun, Y. Qiao, X. Du, *Opt. Laser Technol.* **142**, 107209 (2021)
- S. Bin Humam, G. Gyawali, A. Amanov, T.H. Kim, S.W. Lee, *Surf. Coat. Technol.* **419**, 127293 (2021)
- P. Ke, F. Cai, W.L. Chen, S.Y. Wang, Z.H. Ni, X.H. Hu, M.X. Li, G.H. Zhu, S.H. Zhang, *J. Therm. Spray Technol.* **26**, 857–867 (2017)
- M. Aliofkhaezrai, F.C. Walsh, G. Zangari, H. Köçkar, M. Alper, C. Rizal, L. Magagnin, V. Protsenko, R. Arunachalam, A. Rezvanian, A. Moein, S. Assareh, M.H. Allahyarzadeh, *Appl. Surf. Sci. Adv.* **6**, 100141 (2021)
- F. Liu, C. Liu, X. Tao, S. Chen, *J. Univ. Sci. Technol. Beijing, Miner. Metall. Mater.* **13**, 329–332 (2006)
- S. Hong, J. Qin, J. Lin, Y. Wu, J. Li, Y. Zheng, *J. Mater. Res. Technol.* **21**, 1507–1518 (2022)
- V.V. Satyavathi Yedida, H. Vasudev, *Mater. Today Proc.* **50**, 1458–1464 (2022)
- Y. Wang, E. Hao, Y. An, J. Chen, H. Zhou, *Appl. Surf. Sci.* **547**, 149125 (2021)
- A.R. Govande, A. Chandak, B.R. Sunil, R. Dumpala, *Int. J. Refract. Met. Hard Mater.* **103**, 105772 (2022)
- G. Jie, S. Yan, W. Kangning, S. Qiang, W. Canming, *Surf. Coat. Technol.* **446**, 128761 (2022)
- R. Verma, G. Kaushal, *J. Therm. Spray Technol.* **31**, 2191–2206 (2022)
- X. Yang, R. Zeng, X. Fu, X. Wang, J. Zhou, L. Yu, *Corros. Sci.* **205**, 110408 (2022)
- C. Pan, M. Gong, S. Feng, X. Chen, X. Zhao, P. He, *Surf. Coat. Technol.* **419**, 127278 (2021)
- K. Chong, Y. Zou, D. Wu, Y. Tang, Y. Zhang, *Surf. Coat. Technol.* **418**, 127258 (2021)
- G. Laplanche, A. Kostka, C. Reinhart, J. Hunfeld, G. Eggeler, E.P. George, *Acta Mater.* **128**, 292–303 (2017)
- Q. Pan, L. Zhang, R. Feng, Q. Lu, K. An, A.C. Chuang, J.D. Poplawsky, P.K. Liaw, L. Lu, *Science* **374**, 984–989 (2021)
- B. Gludovatz, A. Hohenwarther, K.V.S. Thurston, H. Bei, Z. Wu, E.P. George, R.O. Ritchie, *Nat. Commun.* **7**, 10602 (2016)
- H. Wang, Z. Hu, J. Cao, S. Zhang, T. Cheng, Q. Wang, *Met. Mater. Int.* **28**, 514–522 (2022)
- J. Miao, C.E. Slone, T.M. Smith, C. Niu, H. Bei, M. Ghazisaeidi, G.M. Pharr, M.J. Mills, *Acta Mater.* **132**, 35–48 (2017)
- S. Pan, C. Zhao, P. Wei, F. Ren, *Wear* **440–441**, 203108 (2019)
- M. Zhu, F. He, Y. Yuan, S. Guo, G. Wei, *Intermetallics* **139**, 107370 (2021)
- J. Wang, W. Li, H. Yang, H. Huang, S. Ji, J. Ruan, Z. Liu, *Corros. Sci.* **177**, 108973 (2020)
- C. Liu, X. Qiu, Z. Wang, J. Peng, *Met. Mater. Int.* (2022).
- G.Y. Koga, A.R.C. Nascimento, F.B. Ettouil, L.C.M. Rodrigues, G. Zepon, C. Bolfarini, C.S. Kiminami, W.J. Botta, R. Schulz, A. Costa e Silva, C. Moreau, F.G. Coury, *Surf. Coat. Technol.* **454**, 129154 (2023)
- J. Qiu, D.D. Macdonald, R. Schoell, J. Han, S. Mastromarino, J.R. Scully, D. Kaoumi, P. Hosemann, *Corros. Sci.* **186**, 109457 (2021)
- T. Dong, L. Liu, G. Li, R. Wang, J. Yuan, Y. Feng, *Surf. Coat. Technol.* **364**, 347–357 (2019)
- G.-H. Meng, B.-Y. Zhang, H. Liu, G.-J. Yang, T. Xu, C.-X. Li, C.-J. Li, *Surf. Coat. Technol.* **344**, 102–110 (2018)
- T.A. Zimogliadova, A.A. Bataev, D.V. Lazurenko, I.A. Bataev, V.A. Bataev, M.G. Golkovskii, H. Saage, T.S. Ogneva, A.A. Rukhtuev, *Mater. Today Commun.* **33**, 104363 (2022)
- J. Du, Y. Li, F. Li, H. Lu, X. Ran, X. Zhang, X. Qi, *J. Alloys Compd.* **889**, 161656 (2021)
- J. Gao, J. Tan, X. Wu, S. Xia, *Corros. Sci.* **152**, 190–201 (2019)
- V. Randle, *Acta Mater.* **47**, 4187–4196 (1999)
- X.L. An, C.L. Chu, L. Zhou, J. Ji, B.L. Shen, P.K. Chu, *Mater. Charact.* **164**, 110323 (2020)
- D. An, T.A. Griffiths, P. Konijnenberg, S. Mandal, Z. Wang, S. Zaefferer, *Acta Mater.* **156**, 297–309 (2018)
- Y. Zhang, H. Wu, X. Yu, J. Liu, D. Tang, *Mater. Charact.* **190**, 112087 (2022)
- M. Kumar, A.J. Schwartz, W.E. King, *Acta Mater.* **50**, 2599–2612 (2002)
- H. Jafari, S. Emami, Y. Mahmoudi, *Appl. Therm. Eng.* **111**, 745–758 (2017)
- P. Bansal, P.H. Shipway, S.B. Leen, *Acta Mater.* **55**, 5089–5101 (2007)
- Z. Zeng, M. Zhou, M. Esmaily, Y. Zhu, S. Choudhary, J.C. Griffith, J. Ma, Y. Hora, Y. Chen, A. Gullino, Q. Shi, H. Fujii, N. Birbilis, *Commun. Mater.* **3**, 18 (2022)
- H. Feng, H.-B. Li, J. Dai, Y. Han, J.-D. Qu, Z.-H. Jiang, Y. Zhao, T. Zhang, *Corros. Sci.* **204**, 110396 (2022)
- A. Wetzel, M. von der Au, P.M. Dietrich, J. Radnik, O. Ozcan, J. Witt, *Appl. Surf. Sci.* **601**, 154171 (2022)
- N. Kumar, M. Fusco, M. Komarasamy, R.S. Mishra, M. Bourham, K.L. Murty, *J. Nucl. Mater.* **495**, 154–163 (2017)
- C.A. Della Rovere, J.H. Alano, R. Silva, P.A.P. Nascente, J. Otubo, S.E. Kuri, *Corros. Sci.* **57**, 154–161 (2012)
- S. Mosayebi, M. Rezaei, Z. Mahidashti, *Colloids Surf. A* **594**, 124654 (2020)
- G.J. Brug, A.L.G. van den Eeden, M. Sluyters-Rehbach, J.H. Sluyters, *J. Electroanal. Chem. Interfacial Electrochem.* **176**, 275–295 (1984)
- Z. Chai, C. Jiang, *Electrochim. Acta* **298**, 616–629 (2019)
- L. Freire, M.J. Carmezim, M.G.S. Ferreira, M.F. Montemor, *Electrochim. Acta* **56**, 5280–5289 (2011)
- H. Luo, S. Zou, Y.-H. Chen, Z. Li, C. Du, X. Li, *Corros. Sci.* **163**, 108287 (2020)
- M.A. Veloz, I. González, *Electrochim. Acta* **48**, 135–144 (2002)
- H. Luo, Z. Li, A.M. Mingers, D. Raabe, *Corros. Sci.* **134**, 131–139 (2018)

58. M.C. Biesinger, B.P. Payne, A.P. Grosvenor, L.W.M. Lau, A.R. Gerson, R.S.C. Smart, *Appl. Surf. Sci.* **257**, 2717–2730 (2011)
59. C. Liu, J. Wu, *Corros. Sci.* **49**, 2198–2209 (2007)
60. Y. Fu, J. Li, H. Luo, C. Du, X. Li, *J. Mater. Sci. Technol.* **80**, 217–233 (2021)
61. L. Wang, D. Mercier, S. Zanna, A. Seyeux, M. Laurent-Brocq, L. Perrière, I. Guillot, P. Marcus, *Corros. Sci.* **167**, 108507 (2020)
62. Y.L. Chou, J.W. Yeh, H.C. Shih, *Corros. Sci.* **52**, 2571–2581 (2010)
63. X. Shang, Z. Wang, F. He, J. Wang, J. Li, J. Yu, *China Technol. Sci.* **61**, 189–196 (2018)
64. J.H. Chang, J.M. Chou, R.I. Hsieh, J.L. Lee, *Corros. Sci.* **52**, 2323–2330 (2010)
65. X. Liu, K. Hu, S. Zhang, T. Xu, L. Chen, E. Byon, D. Liu, *Corros. Sci.* **203**, 110351 (2022)
66. Y. Wang, J. Jiang, Y. Chi, X. Mao, L. Zhu, Y. Dong, Y. Yang, J. He, *Ceram. Int.* **48**, 6933–6941 (2022)
67. F.-Y. Ouyang, C.-H. Chang, B.-C. You, T.-K. Yeh, J.-J. Kai, *J. Nucl. Mater.* **437**, 201–207 (2013)
68. C.-L. Ren, H. Han, W.-B. Gong, C.-B. Wang, W. Zhang, C. Cheng, P. Huai, Z.-Y. Zhu, *J. Nucl. Mater.* **478**, 295–302 (2016)

**Publisher's Note** Springer Nature remains neutral with regard to jurisdictional claims in published maps and institutional affiliations.

Springer Nature or its licensor (e.g. a society or other partner) holds exclusive rights to this article under a publishing agreement with the author(s) or other rightsholder(s); author self-archiving of the accepted manuscript version of this article is solely governed by the terms of such publishing agreement and applicable law.